HIGH FIDELITY MODELLING OF TAPERED LAMINATES WITH INTERNAL PLY TERMINATIONS

L.F. Kawashita[1*], M. Jones[1], S. Giannis[2], S.R. Hallett[1], M.R. Wisnom[1]
[1] Advanced Composites Centre for Innovation and Science, University of Bristol, Bristol, UK
[2] Materials Engineering Research Laboratory (MERL) Ltd., Hitchin, UK
* Corresponding author (luiz.kawashita@bristol.ac.uk)

Keywords: *delamination, ply drop, cohesive element, manufacturing defect*

1. Introduction

Composite structures in aerospace applications often require complex shapes in order to meet aerodynamic and structural requirements. When such components are manufactured from pre-preg material, then internal ply terminations must be introduced in order to allow progressive reductions in thickness. Ply terminations, also known as ply 'drop-offs', generate discontinuities in material properties which result in high stress concentrations upon loading, with linear elastic analyses predicting singular stress fields.

In the absence of other macroscopic defects, the delamination behaviour of tapered laminates is strongly influenced by the configuration of its internal ply terminations. In order to minimise the effect of stress concentrations, the layup must be optimised so that ply drop-offs do not appear in highly stressed regions. Another requirement for optimum performance is the minimisation of interactions between neighbouring ply terminations.

Although some layups can be analysed in two dimensions using closed-form analytical solutions [1], the considerations of three-dimensions, ply drop interactions and nonlinear behaviour are all difficult to address analytically. The modelling of delamination in real tapered laminates therefore requires nonlinear finite element (FE) analyses accounting for the detailed laminate layup and the presence of internal ply drop-offs.

The main objective of the present work was to develop and validate numerical tools which would enable the high-fidelity modelling of complex layups in acceptable time frames. The strategy is based on two main features, namely (i) the use of advanced meshing algorithms to generate realistic ply-by-ply finite element models with internal ply terminations, and (ii) the use of custom cohesive element formulations for the solution of static and fatigue delamination in a dynamic explicit finite element framework.

The resulting methodology provides a virtual testing environment which can be used to quickly evaluate design options and to investigate the influence of manufacturing defects. The tools and techniques developed here are demonstrated and validated via the analysis of a Simplified Ply Drop (SPD) specimen made of carbon/epoxy prepreg material. The virtual testing methodology was used to design the test specimens and to predict their delamination behaviour. Experiments were then conducted under quasi-static and cyclic loading for pristine specimens as well as specimens with artificial delaminations.

2. Experimental Procedures

The simplified ply drop (SPD) specimen was designed to reproduce the delamination behaviour of larger tapered laminates in a simpler and more affordable format. The chosen specimen is shown in Fig. 1. The thin section contains 8 plies while the thick section contains 16 plies, with a nominal cured ply thickness of 0.25 mm. Fig. 2 shows the layup of the specimen, which is $[0°/+45°/0°/-45°]_S$ in the thin section and $[0°/+45°/0°/-45°]_{2S}$ in the thick section, except for two plies which have been swapped to generate a 0° ply termination at the thin end of the tapered region. Ply terminations are interleaved and separated by 2 mm longitudinally.

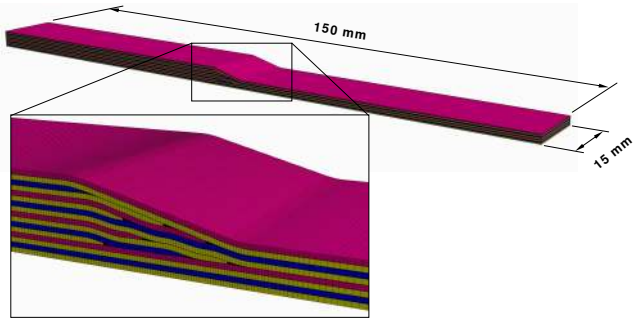

Fig. 1: the Simplified Ply Drop (SPD) specimen.

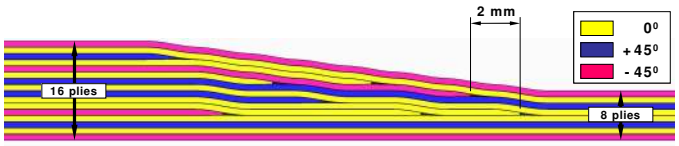

Fig. 2: SPD specimen layup.

Because the tapering is asymmetric, loading of the specimen in axial tension will result in the generation of bending moments as shown in Fig. 3. Therefore a symmetric version of the SPD specimen has also been studied by adhesively bonding back-to-back two laminates with mirrored layups, also shown in Fig. 3.

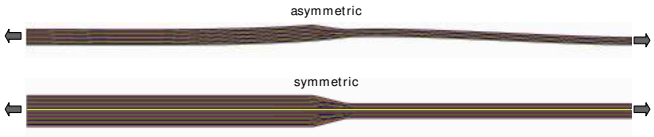

Fig. 3: Asymmetric and Symmetric configurations.

SPD specimens were manufactured using the Hexcel IM7/8552 carbon-epoxy prepreg material on flat tooling and cured in an autoclave. Pristine specimens were manufactured as well as specimens with artificial defects consisting of 15 µm-thick, 4 mm-long strips of fluoropolymer release film running across the full width of the specimens. The artificial defects were embedded in the laminate during the layup process, with their locations being selected by finite element modelling as will be presented in the next sections.

Both specimen configurations (asymmetric and symmetric) in both 'pristine' and 'defect' versions were tested in a LabView-controlled environment consisting of a servo-hydraulic testing machine, contacting extensometers, strain gauges and two digital cameras to detect delaminations on either side of the specimen.

Quasi-static tests were conducted by applying a monotonic axial displacement of 0.5 mm/min until the first unstable delamination growth was detected, with at least 3 repeats for each case. Fatigue tests were conducted by applying sinusoidal loading with a trough/peak ratio (R-ratio) of 0.1 and a frequency of 5 Hz. At least 10 fatigue tests were performed for each case. Different load severities were investigated, between 55% and 85% of the static failure load.

3. Numerical Methods

3.1 Meshing algorithms

Custom algorithms have been written using the Matlab® software package for the generation of ply-level meshes directly from CAD drawings of the specimens. Realistic ply drop geometries and smooth ply curvatures were generated as shown in Fig. 4. The geometries of the ply terminations and resin pockets were controlled by two user-defined parameters, the overall 'ply drop length' l_{PD} and the length of the resin pocket l_{RP}. The ratio between these defined the amount of tapering observed at the terminating ply. These two parameters could be adjusted to produce accurate representations of real resin pockets as shown in Fig. 5. Cohesive elements were inserted automatically between every ply and around resin elements, with the exception of the vertical edge of the terminated ply which was assumed to be pre-cracked in accordance with experimental observations.

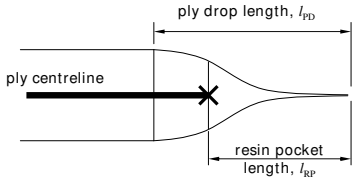

Fig. 4: Idealised geometry of a ply drop.

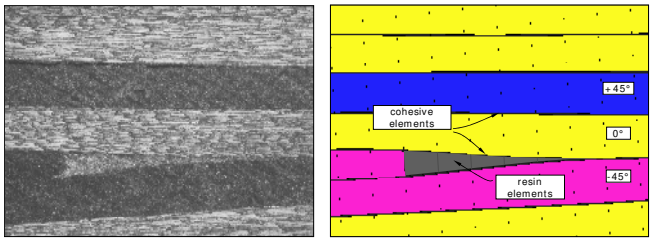

Fig. 5: High fidelity model of a ply termination.

The baseline mesh refinement had minimum element lengths of 0.1 mm in critical zones, coarsening gradually to 3 mm at the extremities of the specimen, with one element through the thickness of each ply. This choice of baseline mesh refinement was backed by various mesh sensitivity studies with up to three elements through the thickness of each ply and element lengths down to 0.05 mm.

3.2 User-defined cohesive elements

3.2.1 Quasi-static formulation

The cohesive formulation adopted in this work is based on the mixed-mode bilinear softening law implemented as 8-noded elements for the explicit finite element solver LS-Dyna [2, 3] . A quadratic damage initiation criterion is used,

$$\sqrt{\left(\frac{\langle \sigma_I \rangle}{\sigma_I^{\max}}\right)^2 + \left(\frac{\sigma_{II}}{\sigma_{II}^{\max}}\right)^2} = 1, \qquad (1)$$

and for propagation a linear interaction of mode-I and mode-II fracture energies,

$$\frac{G_I}{G_{IC}} + \frac{G_{II}}{G_{IIC}} = 1. \qquad (2)$$

3.2.2 Fatigue envelope solution

When modelling fatigue damage accumulation and propagation over large numbers of cycles, it is impractical to analyse each load cycle individually. For constant amplitude loading, one alternative is to perform an analysis of the *envelopes* of load and deformation [4-7]. In this case the number of cycles is assumed to be proportional to the elapsed simulation time, so that fatigue degradation can be computed at each increment based on the length of the time step. Simulation time is then treated as *pseudo-time* since it is no longer related to physical properties such as kinetic energy or strain rate.

The simulation begins with an initialisation step where the load is increased gradually from zero to the peak load in the assumed cyclic regime. After a short stabilisation period, the fatigue degradation law is activated, marking the start of the fatigue analysis. The envelopes of displacements then expand as the interfaces degrade and the interfacial stiffness decreases.

Fatigue degradation is computed for each interface element individually based on the number of cycles and the amplitude in strain energy release rate, as described below.

3.2.3 Fatigue formulation

The baseline fatigue formulation has been described in detail in [6]. In order to account for the degradation due to fatigue loading, we introduce a fatigue damage parameter D_f in the cohesive formulation so that the total accumulated damage becomes,

$$D = D_s + D_f. \qquad (3)$$

During a fatigue analysis D_f increases with an increasing number of fatigue cycles. The evolution of fatigue damage is determined by a modified Paris law for the given material,

$$\frac{da}{dN} = C\left(\frac{\Delta G}{G_C}\right)^m, \qquad (4)$$

where a is the crack length, N is the number of cycles, ΔG is the strain energy release rate amplitude, G_C is the critical strain energy release rate associated with delamination growth, and C and m are the Paris law coefficients obtained from a best fit to experimental data. Paris law coefficients are defined separately for modes I and II, so that effective coefficients C and m can be computed locally at every time step based on the local mode ratio $G_{II}/(G_I + G_{II})$. The peak mixed-mode strain energy release rate amplitude, $G_{\max}$, is obtained via the numerical integration of the mixed-mode stress-displacement history of the element. The amplitude ΔG is calculated from the user-defined load ratio, and from the Paris law a crack growth rate da/dN is obtained. This is then converted into a fatigue damage rate, $\partial D_f / \partial N$, which defines the increment in fatigue damage for the current time step.

The computation of damage rate is based on the crack growth rate da/dN and the length of the interface element in the direction of crack propagation, l_e. The number of cycles for failure of a particular cohesive element is given by,

$$\Delta N_e = \left(\frac{\mathrm{d}a}{\mathrm{d}N}\right)^{-1} l_e. \qquad (5)$$

One can then compute the fatigue damage rate necessary to fail the element in this number of cycles, i.e.,

$$\frac{\partial D_f}{\partial N} = \frac{(1 - D_s)}{\Delta N_e}. \qquad (6)$$

Finally, the updated fatigue damage parameter at time step t is given by,

$${}^{t}D_f = {}^{t-\Delta t}D_f + (\Delta t \cdot f)\frac{\partial D_f}{\partial N}. \qquad (7)$$

where ${}^{t-\Delta t}D_f$ is the damage variable at the previous time step, Δt is the time step size, and f is the loading frequency. The total damage is then computed from Equation (3) and used to retrieve the cohesive tractions for the current time step.

3.2.4 *Crack tip tracking*

As shown in Equation (5), the computation of fatigue damage rate $\partial D_f / \partial N$ is based on the length of a *single* interface element, l_e. This implies that only one element should be under fatigue degradation in the direction of crack propagation at any time. In other words, fatigue degradation should be applied only to the cohesive elements which are part of a crack front.

A crack tip tracking formulation has been developed and is described in detail in [8]. It is based on the use of novel algorithms which enable the identification of elements pertaining to numerical crack fronts, the estimation of the direction of propagation and the mesh-insensitive computation of strain energy release rate amplitude.

3.3 Material Properties

The elastic mechanical properties for unidirectional (UD) laminates of IM7/8552 are summarised in Table 1. For slice models the ±45° plies were modelled using equivalent homogeneous material properties which are listed in Table 2. These properties were obtained from classical laminate theory assuming that these plies behave as if in a $[\pm 45°]_S$ laminate.

Table 3 shows the cohesive strengths which were measured by Hexcel Composites Ltd. [9] and used in the present work. Fracture toughness follow those of [2], taken from [10]. The cohesive stiffnesses E_I and E_{II} were estimated from the isotropic mechanical properties of the resin, i.e. a Young's modulus $E = 4.67$ GPa and Poisson's ratio $\nu = 0.33$ [11], assuming a resin-rich layer of 0.01 mm in thickness.

Table 1: Elastic properties for unidirectional IM7/8552 laminates.

E_{11} [MPa]	E_{22} [MPa]	E_{33} [MPa]	ν_{12}	ν_{13}	ν_{23}	G_{12} [MPa]	G_{13} [MPa]	G_{23} [MPa]
161000	11380	11380	0.32	0.32	0.436	5170	5170	3962

Table 2: Equivalent properties for IM7/8552 plies oriented at ±45°.

E_{11} [MPa]	E_{22} [MPa]	E_{33} [MPa]	ν_{12}	ν_{13}	ν_{23}	G_{12} [MPa]	G_{13} [MPa]	G_{23} [MPa]
18559	18559	13438	0.7949	0.0933	0.0933	41576	4566	4566

Table 3: Cohesive properties for unidirectional IM7/8552 laminates.

G_{IC} [N/mm]	G_{IIC} [N/mm]	σ_I^{max} [MPa]	σ_{II}^{max} [MPa]	E_I [N/mm^3]	E_{II} [N/mm^3]
0.2	1.0	111.0	120.0	4.67×10^5	1.75×10^5

Table 4: Assumed coefficients of thermal expansion for IM7/8552 plies.

α_{11} [mm/°C]	α_{22} [mm/°C]	α_{33} [mm/°C]
0.0	1×10^{-5}	1×10^{-5}

All fatigue analyses employed the Paris-law coefficients shown in Table 5, which were obtained from a best fit to experimental data obtained from DCB and ENF tests assuming the modified Paris-law in Equation (4).

Table 5: Paris law coefficients for unidirectional IM7/8552 laminates (5 Hz, peak/trough ratio of 0.1).

C_I	m_I	C_{II}	m_{II}
1.87389×10^{-4}	16.1478	6.69×10^{-2}	6.37

3.4 Image-Based Meshing

In order to account for any imperfections in the internal positioning of plies or the external specimen geometry, the SPD specimens were re-meshed using an image-based procedure once specimens had been manufactured.

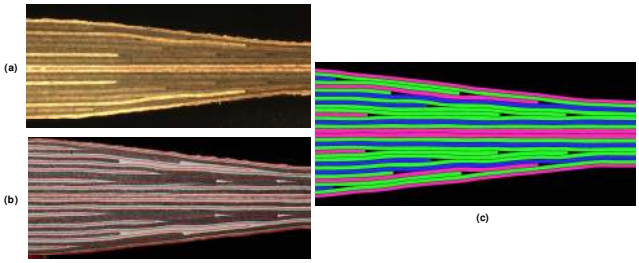

Fig. 6: Image-based meshing of the SPD specimen.

The sides of specimens were manually polished and an optical microscope was used to produce digital images as shown in Fig. 6a. The 0° plies reflected more light and appeared brighter than angled plies. CAD software was then used to digitise the centrelines of each ply and produce series of connected lines, Fig. 6b. The CAD data were then used with the meshing algorithm described previously. This resulted in image-based meshes as shown in Fig. 6c. The shape of the resin pockets was adjusted in order to match experimental observations. The image-based meshing technique accounted for most 'macroscopic' imperfections in the specimen, providing the correct final dimensions, real cured ply thicknesses and real location of ply terminations.

4. Results and Discussion

The delamination behaviour of the SPD specimen is described here in terms of the various ply interfaces and internal ply terminations shown in Fig. 7. Ply drop-offs are numbered according to their position along the length direction, from the thin to the thick section, and the three interfaces at each ply drop are identified with letters a, b and c.

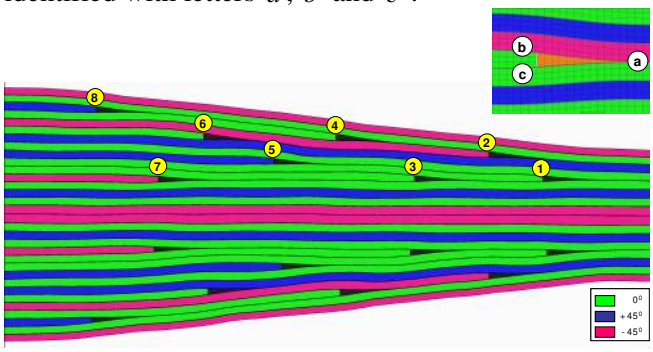

Fig. 7: Ply drop off numbers and interfaces.

4.1 Quasi-static loading

Results of quasi-static tests on asymmetric and symmetric specimens are shown in Fig. 8 and Fig. 9, respectively. The scatter in experimental results was relatively low with standard deviations (SD) of 0.6 kN and 1.2 kN for asymmetric and symmetric specimens, respectively. Good agreement was observed between experimental and numerical results both in terms of delamination load and initiation locus. Delamination initiated along interfaces 1b and 1c for all pristine specimens.

4.2 Artificial Defect Locations

The meshing algorithm was automated for the batch analysis of inserted delaminations at various locations. Because this study preceded the manufacture of SPD specimens, nominal dimensions were used instead of an image-based meshing procedure. The embedded release film was modelled as a frictionless contact and its possible locations were defined according to the interface numbering shown in Fig. 7. Therefore 24 different cases were analysed for each specimen configuration. The results for asymmetric specimens are shown in Fig. 10, and the worst defect location in this case is interface 1b. Fig. 11 shows similar results for the symmetric specimen configuration, the critical location in this case being interface 2a.

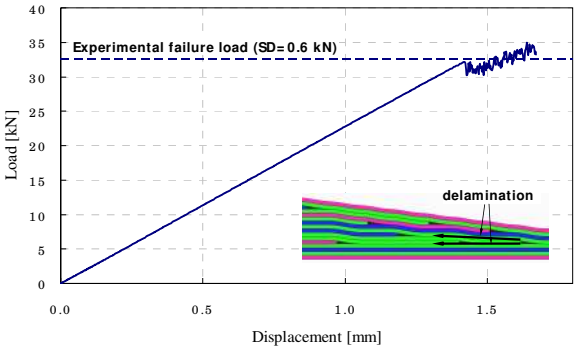

Fig. 8: Quasi static results for asymmetric specimens.

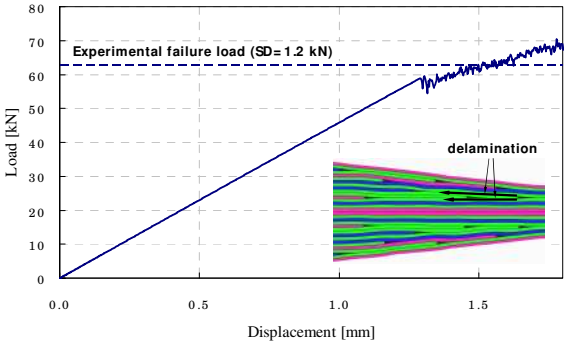

Fig. 9: Quasi static results for symmetric specimens.

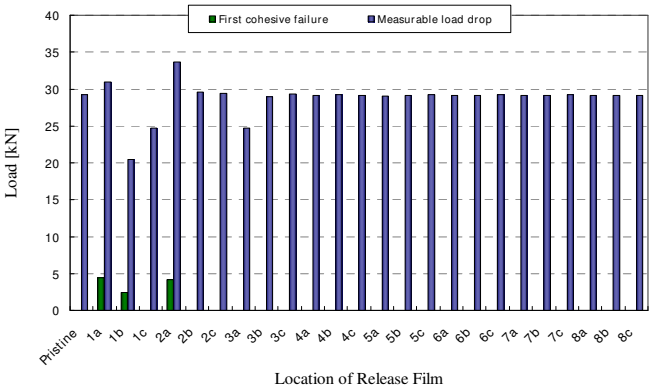

Fig. 10: Analysis of asymmetric specimens with defects.

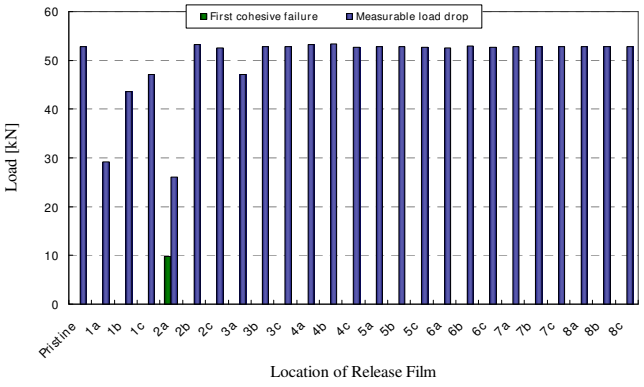

Fig. 11: Analysis of symmetric specimens with defects.

4.3 Fatigue loading

Results of fatigue tests and simulations are presented in terms of modified S-N curves relating the peak applied thin section stress with the number of cycles to the onset of delamination. For numerical results, this onset is defined as the appearance of a 1 mm long delamination, while in experiments it is the first observable crack. Results for the asymmetric specimen are shown in Fig. 12. A good agreement is observed between model predictions and experimental results for specimens with and without embedded defects.

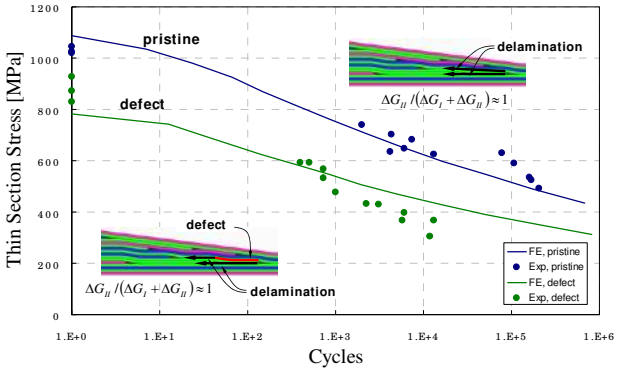

Fig. 12: Fatigue S N curves for asymmetric specimens.

Fatigue results for symmetric specimens are shown in Fig. 13. Good agreement was observed for pristine specimens. For specimens with defects, the nearly pure mode-I delamination and the extremely 'steep' Paris law for the material in mode-I (Table 5) meant that, for the meshes investigated here, the models predicted either very fast delamination growth or complete run-out for severities between 85-95%. Therefore further work is required in order to avoid the need for extremely refined meshes.

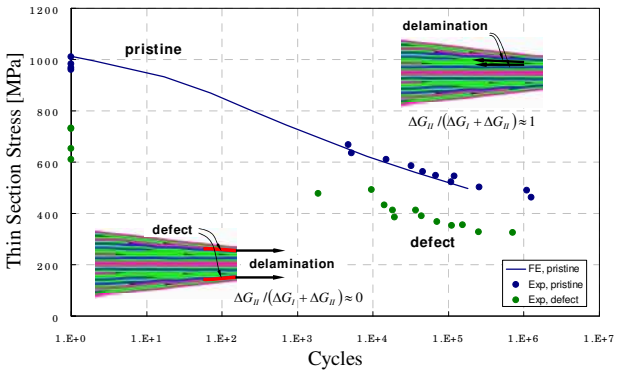

Fig. 13: Fatigue S N curves for symmetric specimens.

5. Conclusions

A methodology has been developed for the analysis of delamination in tapered laminates under static and fatigue loading. This is based on the use of ply-by-ply FE models with custom (user defined) cohesive elements between every ply. Good correlation was observed between model predictions and experimental measurements in terms of delamination location, delamination load (quasi-static) and delamination growth (fatigue). These tools have then been used to study and analyse the effect of embedded artificial delaminations, simulating manufacturing defects.

Acknowledgements

Rolls-Royce plc. and the UK Technology Strategy Board are acknowledged for their support of this research.

References

[1] G. Allegri, M.R. Wisnom, S.R. Hallett; Composites Part A, Vol. 41, Iss. 10, pp. 1388-1394, 2010.

[2] Jiang WG, Hallett SR, Green BG, Wisnom MR; *Int J Num Meth Eng*; v. 69, iss. 9, pp. 1982-1995 (2007).

[3] Li X, Hallett SR, Wisnom MR; *Composites Part A*; volume 39, issue 2, pages 218-230 (2008).

[4] Robinson P, Galvanetto U, Tumino D, Bellucci G, Violeau D; *Int J Num Meth Eng*, v. 63, iss. 13, pp. 1824-1848 (2005).

[5] Turon A, Costa J, Camanho PP, Davila CG; *Composites Part A*, v. 38, pp. 2270–2282 (2007).

[6] Harper P W, Hallett S R; *International Journal of Fatigue*, vol. 32, no. 11, pp. 1774–1787 (2010).

[7] Kawashita LF, Jones MI, Trask RS, Hallett SR, Wisnom MR; *Proceedings of the ICCM17*, Edinburgh, UK, 2009.

[8] Kawashita LF, Hallett SR; "Crack tip tracking formulation of cohesive elements for mesh insensitive analysis of fatigue delamination"; *Manuscript in preparation* (2011).

[9] Lee J, Soutis C; *Composites Science and Technology*, 68(12):2359–2366 (2008).

[10] Jiménez MA, Miravete A.; *Journal of Composite Materials*; 38:1309–1335] (2004).

[11] HexPly® 8552 Product Data, *Hexcel Composites* (2008).